Chapter 2

OPERANDO SYNTHESIS OF MACROPOROUS MOLYBDENUM DISELENIDE FILMS FOR THE ELECTROCATALYSIS OF THE HYDROGEN-EVOLUTION REACTION

Saadi, F. H.; Carim, A. I.; Velazquez, J. M.; Baricuatro, J. H.; McCrory, C. C.; Soriaga, M. P.; Lewis, N. S. *ACS Catalysis* **2014**, *4*, 2866. DOI: http://10.1021/cs500412u

2.1 Introduction and Motivation

Shortly before I began my doctorate, Group VI chalcogenides were discovered as promising catalysts for the hydrogen evolution reaction and stable in acidic media.[1] Group VI chalcogenides such as molybdenum disulfide (MoS_2), molybdenum diselenide ($MoSe_2$), tungsten disulfide (WS_2), and tungsten diselenide (WSe_2) are comprised of earth-abundant elements, are stable in strong acid, and catalyze the HER with reported overpotentials of ~200-350 mV to produce current densities of -10 mA cm^{-2}.[1-25] Theoretical[3, 11] and experimental[1] studies of MoS_2 crystals suggest that the $<10\bar{1}0>$ edge sites are the active sites for hydrogen evolution. Many methods of preparing catalytically active MoS_2 have been developed, including sulfurization of molybdenum,[19] electrochemical deposition from ammonium thiomolybdate,[22, 26] wet-chemical

techniques[5], and *ex crystallum* mechanical exfoliation.[17, 27] In contrast, relatively few methods of preparing catalytically active $MoSe_2$, such as the selenization of metallic molybdenum, have been disclosed.[19, 20]

In this chapter, we describe a two-step method for the synthesis of $MoSe_2$ films that are stable in acid and capable of catalyzing the HER. This method extends to $MoSe_2$, a synthetic route that has been reported for MoS_2.[5, 8] In the first step, wet-chemical techniques are used to form a mixed-composition precipitate, which is then deposited as a film onto electrodes. The film-covered electrodes are then introduced into aqueous acid and used to drive the HER. The as-prepared films exhibited low catalytic activity, but the activity improved under the conditions of the HER, which convert the mixed-composition film into a macroporous film of $MoSe_2$.

2.2 Results

2.2.1 Characterization of as-deposited films

Figure 2.1A and 2.1B show scanning electron micrographs (SEMs) of a mixed-composition film on a glassy carbon substrate. The deposition was non-uniform and consisted of multiple islands ~100 μm in diameter separated by crevices up to 50 μm in width. Each island, however, was smooth and nonporous.

In comparison, Figures 2.1C and 2.1D show SEMs after reductive conversion of the films to HER catalysts during the electrochemical experiments. Substantial changes to the surface terrain were evident relative to the terrain in the pre-electrochemistry images. The island structures that were prominent at low levels of magnification prior to

conversion of the films were no longer visible, and the film appeared to be smooth. However, a macroporous structure that was absent prior to conversion of the films was apparent at higher magnification levels, and covered the entire sample. The pore sizes were estimated to be ~ 200 nm in diameter.

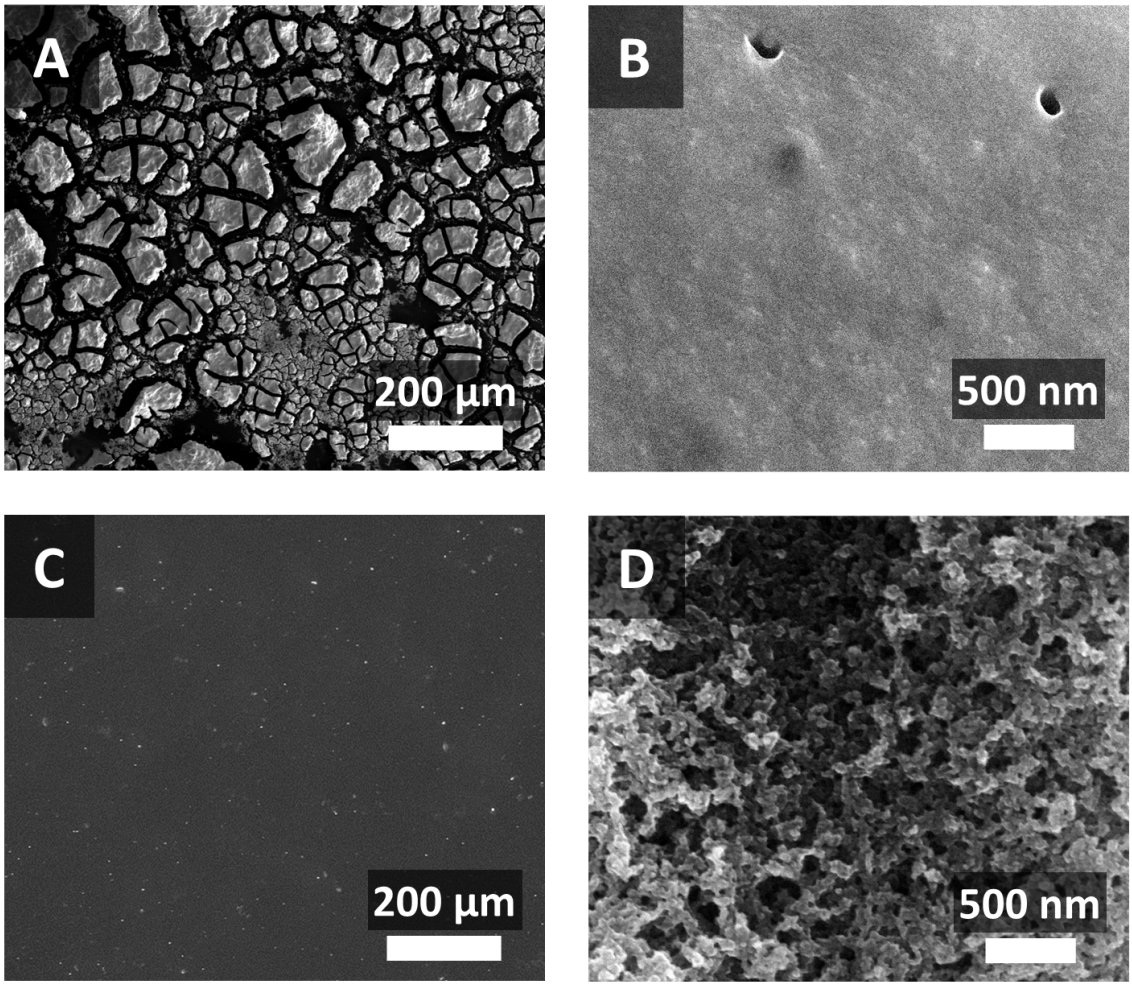

Figure 2.1: Scanning electron micrographs of the films before (A,B) and after (C,D) 10 cycles. (A) The as-deposited mixed-composition films on glassy carbon substrates were non-uniform, consisting of multiple islands ~100 ¦ m in diameter. (B) The surfaces of the islands were relatively smooth. (C) The island structure was not visible after electrocatalysis, and (D) at higher magnification, the entire surface appeared porous.

Figure 2.2A and 2.2B present high-resolution composite XPS spectra of the samples in the Mo and Se regions. Two sets of doublet peaks for Mo were observed (Figure 2.2A). The first doublet consisted of signals for Mo $3d_{5/2}$ at 233 eV and Mo $3d_{3/2}$ at 236 eV, and is characteristic of MoO_3.[4, 28] The second doublet consisted of peaks for Mo $3d_{5/2}$ at 232 eV and Mo $3d_{3/2}$ at 235 eV, and was located in a region typically associated with Mo^{6+}.[29] The single peak at 230 eV is characteristic of Se 3s. Figure 2.2B displays the Se region with two sets of 3d doublets: the higher-energy doublet ascribable to Se^0 and the lower-energy doublet ascribable to Se^{2-}.[30, 31] Quantitation of the Mo $3d_{5/2}$ peak at 232 eV and the Se^{2-} 3d peak at 54 eV yields a Mo:Se ratio of 1:3.

The high-resolution X-ray photoelectron spectra of the Mo 3d and Se 3d regions for the converted films are displayed in Figures 2.2C and 2.2D. The Se 3s signal at 230 eV remained unchanged from the pre-conversion spectra, but the rest of the peak profile in Figure 2.2C was clearly different after the electrochemistry. The intensities of the Mo^{6+} doublet at 232 eV and 235 eV were significantly reduced, and the Mo^{4+} doublet[30] predominated the spectrum at 228.6 eV and 232 eV. More significantly, the Mo^{6+} peaks ascribed to MoO_3 were extinguished after electrolysis. The Se^{2-} species in Figure 2.2D were, therefore, associated with both Mo^{4+} and Mo^{6+} species in the form of $MoSe_2$ and $MoSe_3$. The Se^0 doublet, which was prominent in the pre-conversion spectra (Figure 2.2B), decreased significantly after electrolysis, whereas the doublet attributed to Se^{2-} increased.

It is important to note that, before electrolysis, the O 1s peak (Figure 2.3E) appeared at 530.7 eV; the same O 1s peak was observed for both the oxided molybdenum standards, MoO_3 (Figure 2.3B) and MoO_2 (Figure 2.3D). After electrolysis, the O 1s peak

shifted positively to 532 eV, implying the presence of adventitious oxygen, not of oxygen associated with oxided molybdenum species.

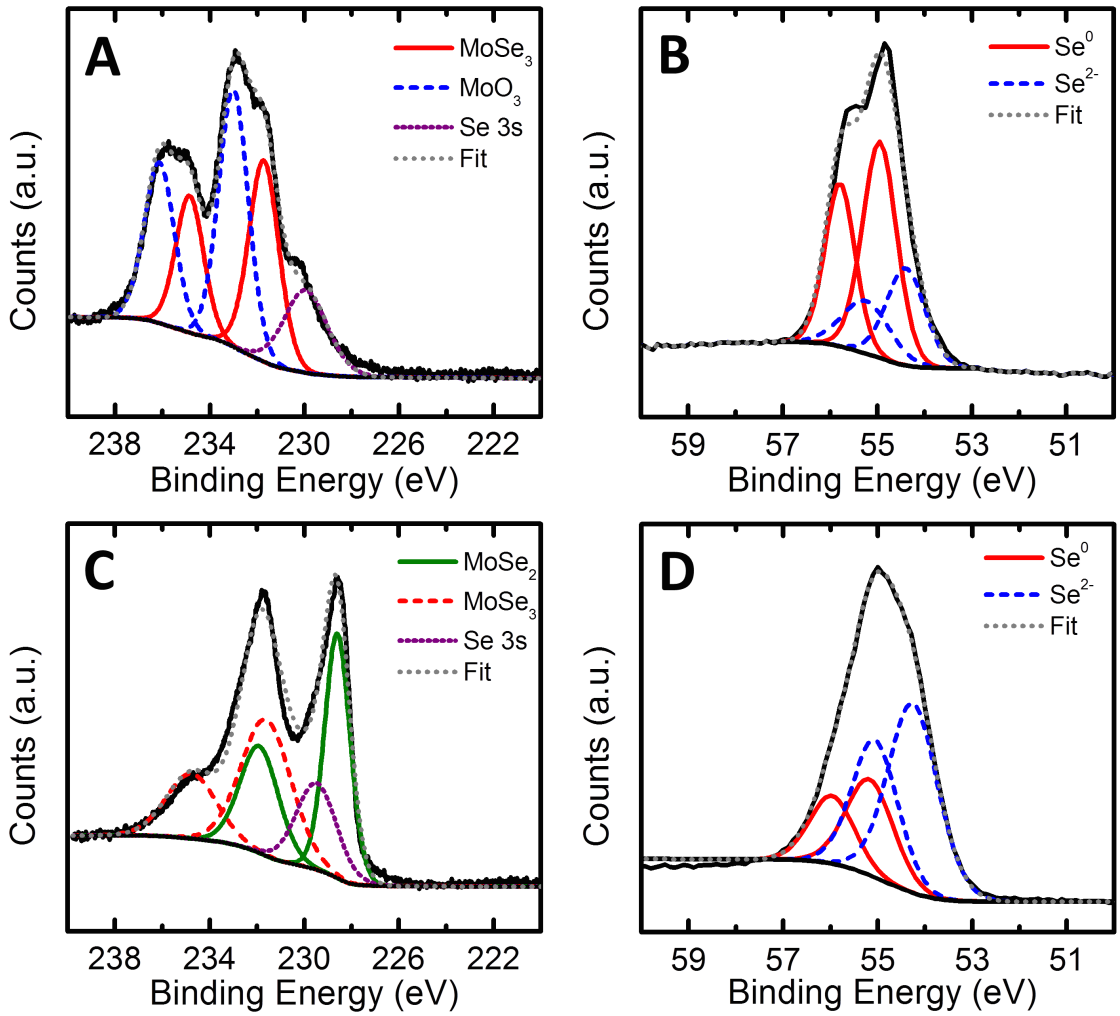

Figure 2.2: High-resolution X-ray photoelectron spectra of (A) the Mo 3d region of an as-deposited thin film; (B) the Se 3d region of an as-deposited thin film; (C) the Mo 3d region after 10 cycles; (D) the Se 3d region after 10 cycles.

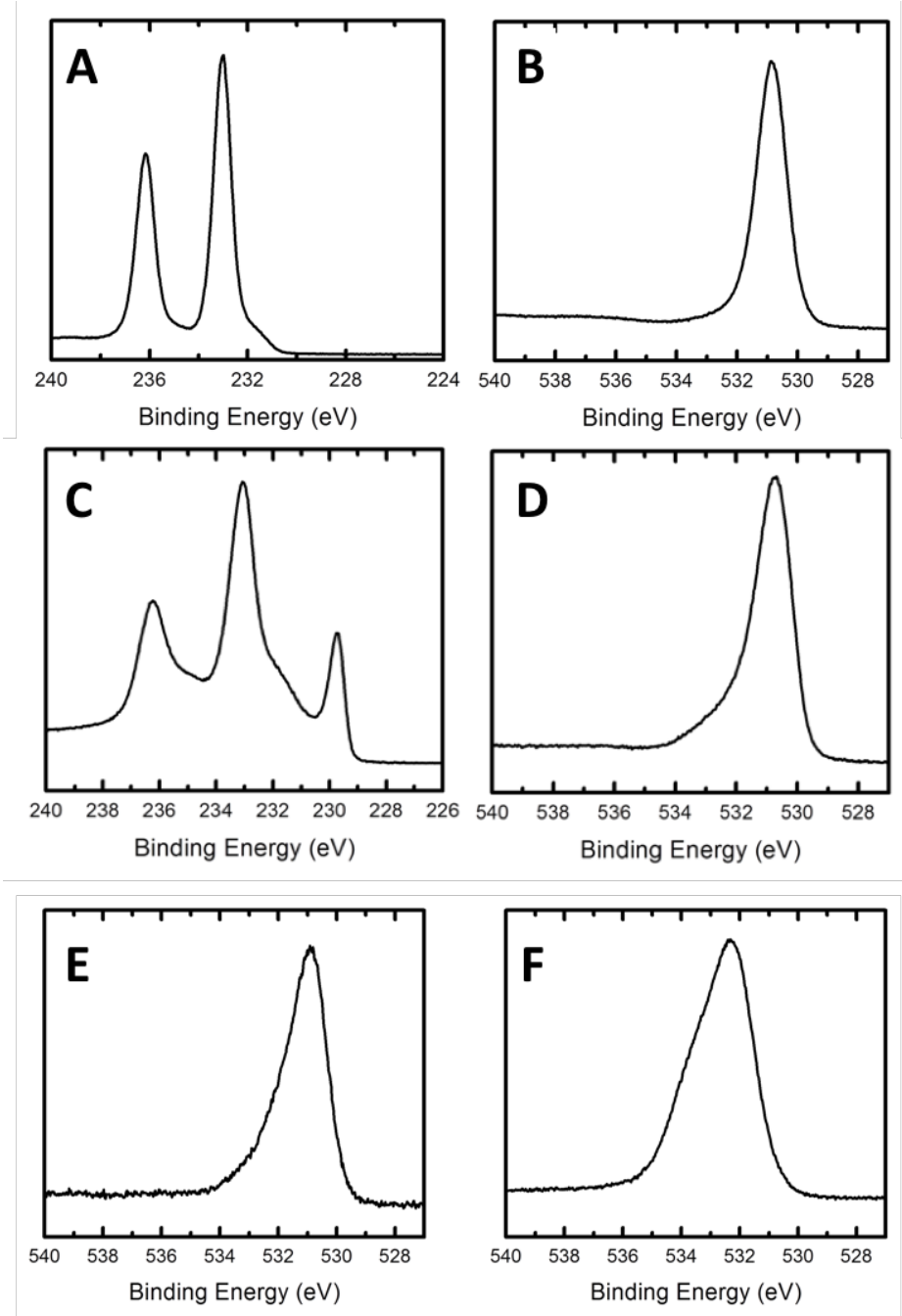

Figure 2.3: High-resolution X-ray photoelectron spectra of (A) the Mo 3d region of MoO_3; (B) the O 1s region of MoO_3; (C) the Mo 3d region of MoO_2; (D) the O 1s region of MoO_2; (E) the O 1s region of the as deposited film; (F) the O 1s region after 10 cycles.

The Raman spectrum of the as-deposited thin film exhibited a broad, asymmetric band centered at 255 cm^{-1} and a shoulder at ~ 238 cm^{-1} (Figure 2.4). The prominent, higher-frequency peak is characteristic of a Se–Se stretch mode in glassy, loosely packed polymer chains, whereas the lower-energy shoulder is also due to a Se–Se stretch vibration, but indicates closely packed chains in which the local microscopic structure resembles that of crystalline (trigonal) Se.[32]

After electrochemistry, the Raman spectra also exhibited significant (Figure 2.4). The vibrational band centered at ~255 cm^{-1}, which was prominent in the as-prepared films, was not observed for the converted films, suggesting that the amorphous polymeric chains of elemental Se were removed from the film during the reductive conversion process. No vibrational peaks characteristic of crystalline molybdenum selenide were detected for the converted films, suggesting that the films remained non-crystalline.

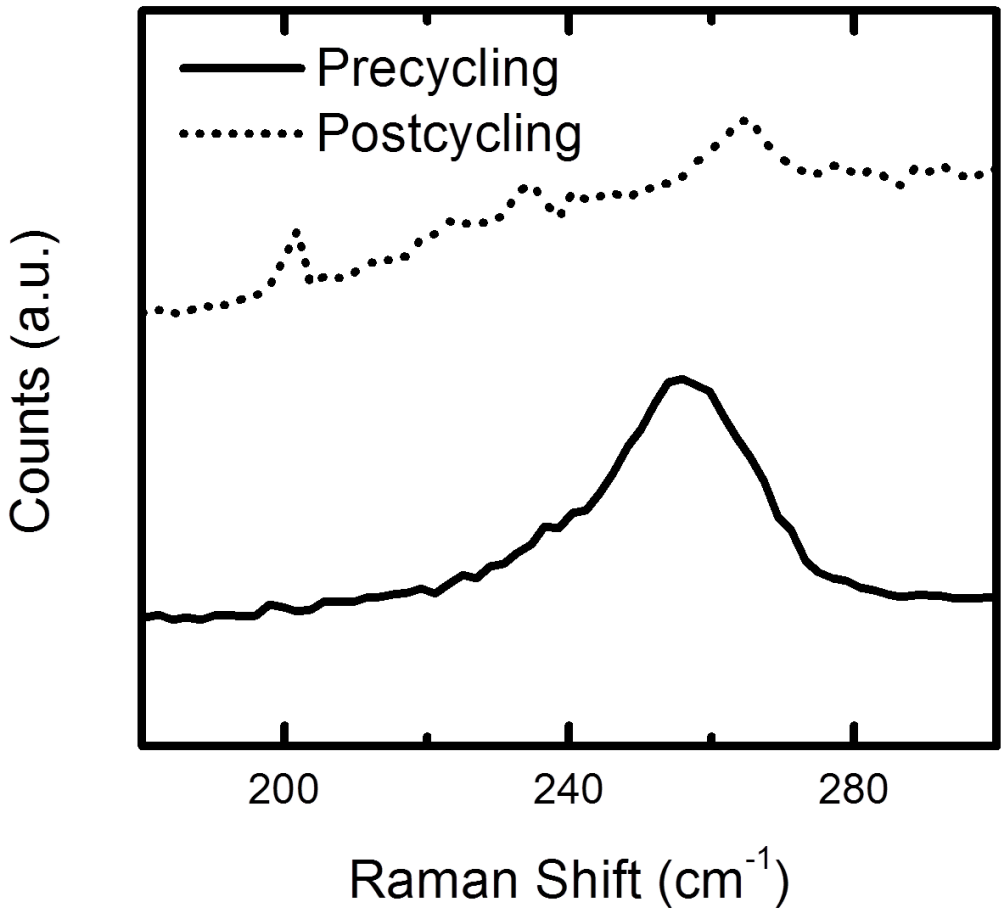

Figure 2.4: Raman spectra of an as-deposited thin film (solid) and of a film after ten cycles (dashed). Prior to voltammetric cycling, a broad, asymmetric band centered at 255 cm^{-1} and a smaller shoulder at 238 cm^{-1} were visible, and are assigned to a Se–Se stretch mode in glassy, loosely packed polymer chains and to a Se–Se stretch vibration of closely packed chains, respectively. These bands were not observed after voltammetric cycling.

Figure 2.5 shows the current density versus scan rate data that were used to calculate the geometric capacitance of a typical mixed-composition thin film and the converted films. The geometric capacitance of the film mixed-composition thin was 120 $\mu F\ cm^{-2}$ and the roughness factor of the film was ~ 2. The geometric capacitance of the converted film was 1200 $\mu F\ cm^{-2}$ and the roughness factor of the film was ~ 20, an order of magnitude larger than that measured in the as-deposited thin film.

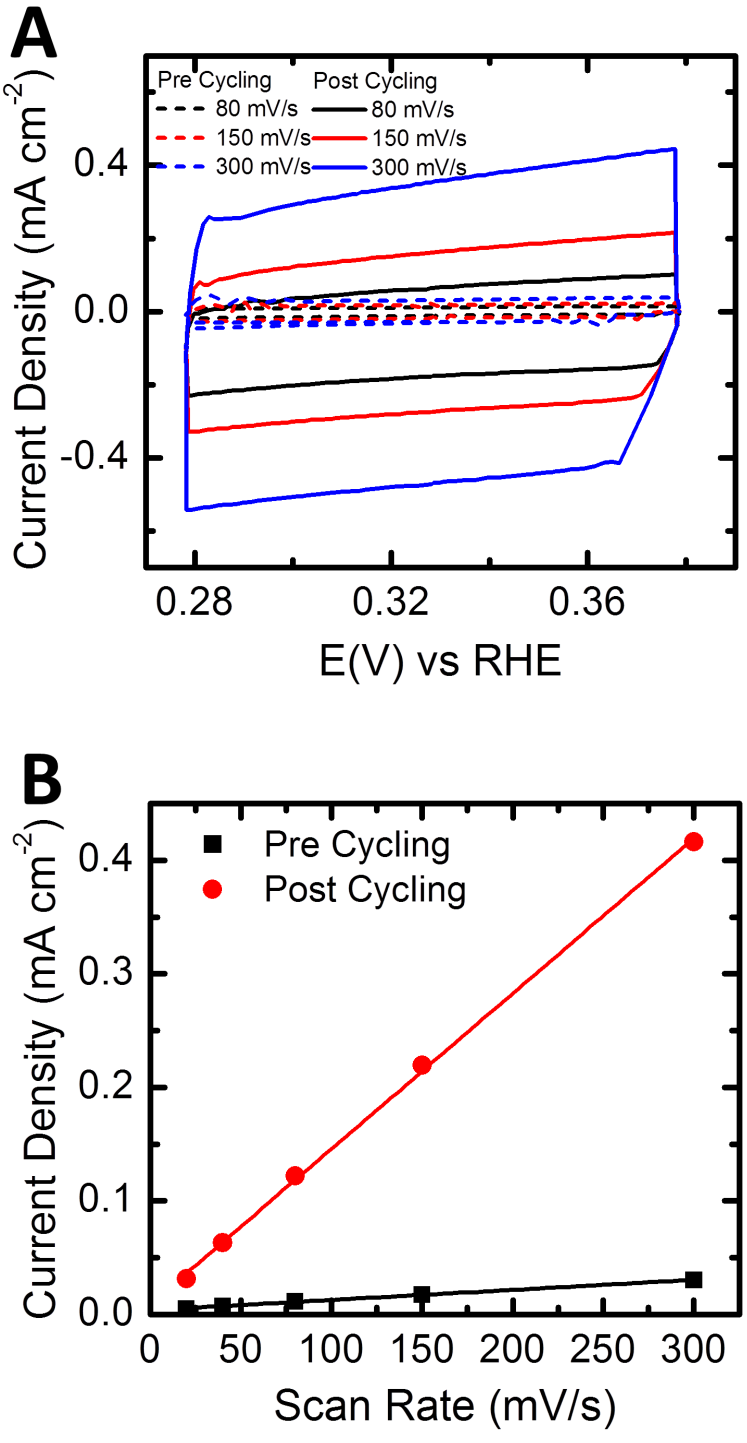

Figure 2.5: Electrochemically active surface area measurements before (pre-cycling) and after (post-cycling) the electrocatalysis experiments shown in Figure 2.6. (A) Cyclic non-

faradaic-current vs potential curves at pre-selected scan rates; (B) Non-faradaic current as a function of the potential scan rate.

2.2.2 Conversion of the films to catalysts of the HER

Figure 2.6A shows the first and tenth cyclic voltammetric cycles obtained using the film-coated glassy carbon RDEs. The onset for hydrogen evolution clearly shifted to less negative potentials between the first and tenth cycles. A steady state was reached by the tenth cycle, at which point 250 mV of overpotential was needed to produce a current density of -10 mA cm^{-2}. Based on the steady-state negative potential sweep data illustrated in Figure 2.5B, the Tafel slope was determined to be 80 mV dec^{-1} with an exchange current density of 1×10^{-5} mA cm^{-2} (Figure 2.6C).

The stability of the prepared film was characterized by plotting the overpotential required to produce a current density of 10 mA cm^{-2} for each cyclic voltammetric sweep performed during 48 h. As shown in Figure 2.6D, the overpotential to produce -10 mA cm^{-2} for the HER increased by ~ 50 mV over 48 h of operation.

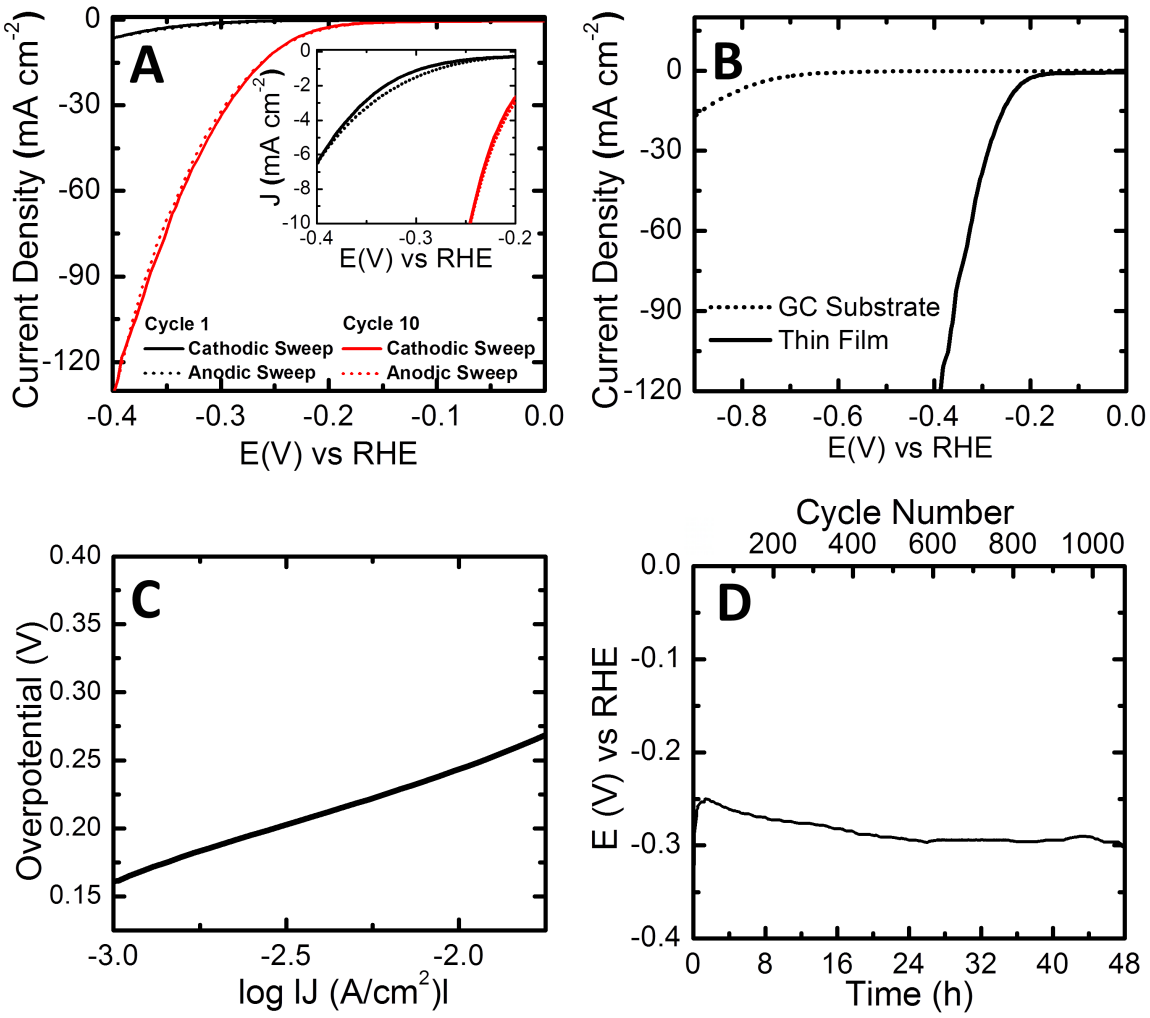

Figure 2.6: (A) Cyclic voltammetric data for molybdenum selenide thin films on glassy carbon in 0.10 M H_2SO_4(aq). In the first cycle, the initial cathodic portion showed a lower current density than the return anodic half-cycle. The current density increases in subsequent cycles, until the tenth cycle when the current density reached steady-state. (B) Current-potential plot for the glassy carbon substrate (dotted curve) and immediately after the tenth (solid curve) cycle. (C) Tafel plot of the current-potential data in (B); (D) A plot of the overpotential needed to produce a current density of 10 mA cm^{-2} data as a function of time.

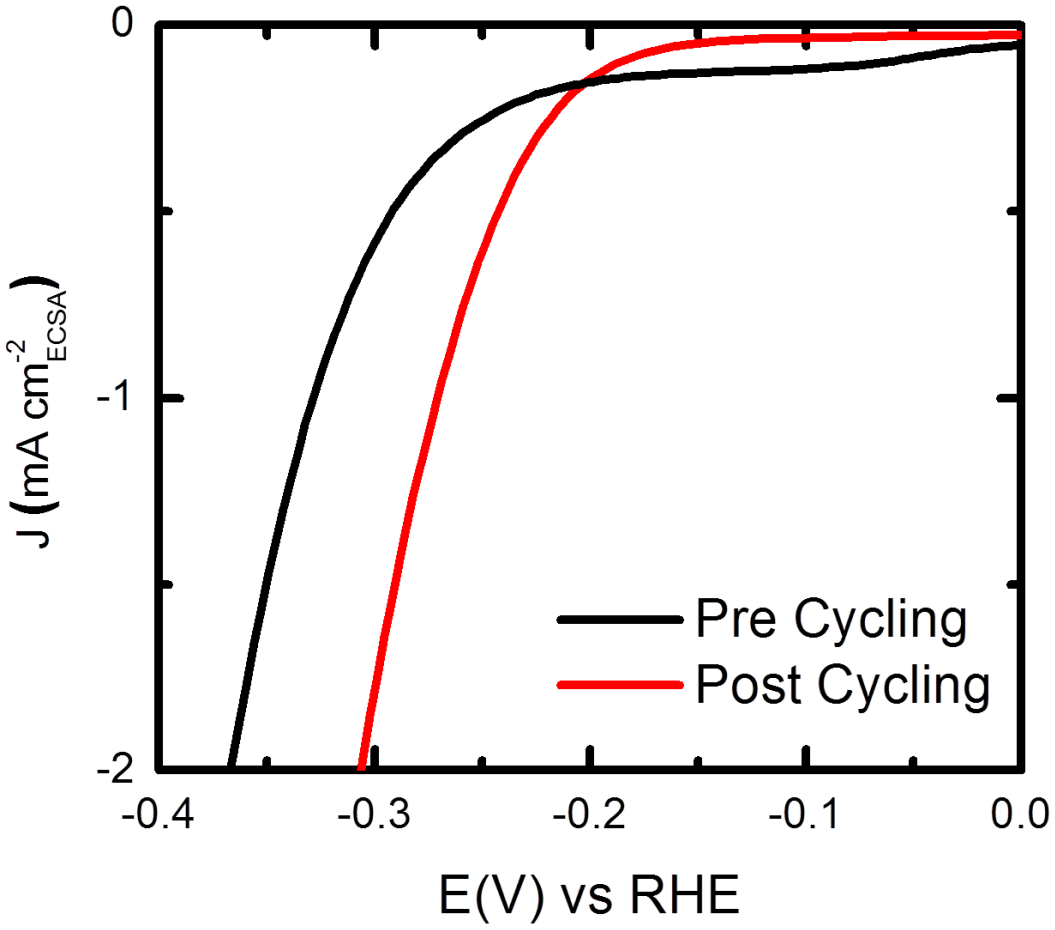

Figure 2.7: Current density-potential profile of the prepared film before (pre-cycling) and after (post-cycling) electrolysis. Normalization of the current density to the electrochemically active surface area gives rise to two distinct polarization curves that show fundamental differences in the catalytic activity of $MoSe_3$ and $MoSe_2$.

2.3 Discussion

Reaction pathways directly analogous to those reported[33-35] for MoS_2 likely apply to the wet-chemical synthesis of the mixed-composition precipitate. In aqueous solutions, ammonium heptamolybdate, $(NH_4)_6Mo_7O_{24}\cdot H_2O$, exists as ammonium orthomolybdate, $(NH_4)_2MoO_4$, a strong electrolyte.[36] Mo is hexavalent in both of these structures. Thus, when sodium selenide is added to an acidic solution of $(NH_4)_6Mo_7O_{24}\cdot H_2O$, the reaction that generates the black precipitate is likely to be:

$$MoO_4^{2-} + 3H_2Se \rightarrow MoSe_3 + 2OH^- + 2H_2O \qquad (2.1)$$

where $MoSe_3$ is the black solid. The XPS data (Figures 2.2A and 2.2B) support the presence of Mo^{6+} and Se^{2-} in the as-prepared films. The same set of XPS data also indicates the presence of MoO_3, which may be formed either under the present synthesis conditions or by exposure of the synthesized $MoSe_3$ to air:

$$2MoSe_3 + 3O_2 \rightarrow 2MoO_3 + 6Se \qquad (2.2)$$

Equation (2.1) may also be accompanied, to a small extent, by the decomposition of $MoSe_3$:

$$MoSe_3 \rightarrow MoSe_2 + Se \qquad (2.3)$$

The Se produced from reactions (2.2) and (2.3) was detected by the XPS and Raman spectroscopy.

$MoSe_2$, which is believed to be an active catalyst for the HER, is present only at very low concentrations, if at all, in the unconverted films, which consist of a mixture of $MoSe_3$, MoO_3, and Se. The as-prepared films are therefore relatively inactive HER catalysts. Reductive cycling significantly improved the catalytic activity of the films

(Figure 2.6A), and a steady state was achieved after ten cycles. This behavior is consistent with a process in which exposure of the multicomponent film to negative potentials, and consequent reductive generation of $H_2(g)$, also served to concentrate $MoSe_2$, based on a combination of three interfacial reactions that are analogous to the known reactions of MoS_2 and H_2S:[33, 37, 38]

$$H_2 + Se \rightarrow H_2Se \quad (2.4)$$

$$MoSe_3 + H_2 \rightarrow MoSe_2 + H_2Se \quad (2.5)$$

$$MoO_3 + 3H_2Se \rightarrow MoSe_2 + 3H_2O + Se \quad (2.6)$$

These reaction schemes are supported by the post-electrochemistry surface analysis: (i) the XPS results (Figure 2.2C and 2.2D) showed a decrease of the MoO_3 and $MoSe_3$ peaks and an emergence of the $MoSe_2$ signal, and (ii) the Raman spectrum (Figure 2.3) did not exhibit the vibrational mode for amorphous elemental Se.

The observed increase in the porosity and surface area of the film (Figure 2.4) may be due to several factors such as the expulsion of gases like H_2 and H_2Se. The release of H_2Se, represented in reaction (2.4), is analogous to the formation of H_2S that accompanies the reduction of MoS_3 to MoS_2 [39, 40]. Material loss due to the dissolution of MoO_3 could also contribute to the observed porosity.

Figure 2.7 plots the current divided by electrochemically active surface area versus potential of the samples before and after ten cyclic voltammagrams. Notably, the improvement in catalytic activity of the material cannot be attributed solely to the increase in internal surface area of the film; i.e., the catalytic activity of the film was still superior after voltammetry even when increase in electrochemically active surface area was accounted for.

The overpotential for the onset for hydrogen evolution was measured to be ~150 mV (Figure 2.6A). The overpotential necessary to effect a HER current density of -10 mA cm^{-2}, a heuristic benchmark to assess catalytic activity in solar fuels applications under unconcentrated sunlight, was <250 mV (Figure 2.6B), and is within the range that has been reported for MoS_2 HER catalysts (~200–350 mV).[4-6, 8, 9, 19, 26] The porous $MoSe_2$ films had higher catalytic activity and a lower Tafel slope than thin films of $MoSe_2$ synthesized via the selenization of Mo on glassy carbon, which required an overpotential of 430 mV to achieve a current density of -8 mA cm^{-2}, reported a Tafel slope of 105-120 mV dec^{-1} and stability for over 1000 cycles.[19, 20]

Although Faradaic yields have not been determined directly, competing cathodic processes are unlikely. Stoichiometric reactions involving Mo or Se cannot have contributed more than 1 % to the charge passed during a 24 h chronoamperometric experiment as detailed in the experimental section.

The macroporous $MoSe_2$ thin films were stable catalysts of the HER in acidic media, and the overpotential required to sustain a current density of -10 mA cm^{-2} only increased by 50 mV over 48 h. Although a comparison of stability across catalysts is not straightforward, due to the wide range of results that have been reported, the macroporous thin film $MoSe_2$ catalysts appear to be at least as stable over the same time period as MoS_2 HER catalysts.[5]

2.4 Conclusion

The catalytically inactive components of a $MoSe_3/MoO_3$ film have been converted, through an *operando* method of synthesis, to produce a catalyst for the HER

while the film is catalyzing the HER. The addition of excess sodium selenide to ammonium heptamolydbate in aqueous sulfuric acid resulted in the spontaneous formation of a black precipitate that consisted primarily of molybdenum triselenide ($MoSe_3$) with small amounts of elemental Se. Molybdenum trioxide (MoO_3) was also formed upon exposure of the triselenide to atmospheric oxygen. The multicomponent thin film cast onto glassy carbon was relative inactive for the HER during initial voltammetric cycles, because the active catalyst, $MoSe_2$, was either not present or was present only at very low concentrations. Further voltammetric cycling of the electrode in the potential region where the HER occurs led to substantial increases in the catalytic activity. By the tenth cycle, the overpotential needed to drive a catalytic current of -10 mA cm^{-2} had decreased from ~450 mV to 250 mV. The improvement in the catalytic activity occurred because, under HER conditions, the catalytically inactive components of the film were reductively converted to $MoSe_2$. An *operando* synthesis of $MoSe_2$ was thus established. An amorphous, macroporous $MoSe_2$ framework was also generated in the synthesis and the $MoSe_2$ film exhibited long-term stability with only a 50 mV increase in overpotential after 48 h of continuous operation. The porous $MoSe_2$ films appear to hold promise as a catalyst for the HER in aqueous acidic electrolytes.

2.5 Experimental

All chemicals and materials were used as received, and all experiments were performed under ambient laboratory conditions, except where otherwise noted. Water was obtained from a Barnstead Nanopure purification system (Thermo Scientific,

Asheville, NC) and had a resistivity ≥ 18.2 MΩ·cm. All glassware was thoroughly cleaned in hot chromic acid (3% potassium dichromate in 10 M H_2SO_4).

Mixed-composition suspension. 0.60 g (5.2 x 10^{-4} mol) of ammonium heptamolybdate, $(NH_4)_6Mo_7O_{24}\cdot 4H_2O$, (99.98%, Sigma Aldrich, St. Louis, MO) was dissolved in 12 mL of a 0.20 M H_2SO_4 solution prepared by diluting 18 M H_2SO_4 (Sigma Aldrich) with H_2O. A separate solution was prepared by dissolving 0.15 g (1.2 x 10^{-3} mol) of sodium selenide, Na_2Se, (99.8%, Alfa Aesar, Ward Hill, MA) in 12 mL of H_2O. Inside a fume hood, the first solution was quickly poured into the second solution, and a black precipitate formed upon mixing.

The suspension was transferred to a centrifuge tube and centrifuged at 12,000 rpm for 30 min using a JA-17 rotor (Beckman Coulter, Brea, CA). A black precipitate collected at the bottom of the centrifuge tube. The yield was calculated to be 70%. The clear supernatant liquid was discarded and the precipitate was rinsed with several 15 mL aliquots of isopropanol (99.7%, Macron Chemicals, Center Valley, PA). A final 15 mL of isopropanol was then added to the centrifuge tube, which was then subjected to 30 min of sonication. This process resulted in suspension of the black solid in the isopropanol.

Preparation of film-coated rotating-disk electrodes (RDEs). Glassy carbon discs (HTW Hochtemperatur-Werkstoff GmbH, Thierhaupten, Germany), 5 mm in diameter and 4 mm thick, were polished on a LaboPol-5 polishing wheel (Struers, Inc., Cleveland, OH), first with a 600-grit Carbimet SiC grinding paper (Buehler, Lake Bluff, IL) for 30 s, and subsequently with diamond slurries (Buehler) of 9, 6, 3, 1, and 0.1 μm diamond particle size, also for 30 s each. The carbon disks were then cleaned by sonication for 5

min *seriatim* in isopropanol (Macron Chemicals), acetone (ACS grade, Sigma Aldrich) and water.

A 30 μL drop (mass loading of 1.36 mg cm^{-2}) of the mixed-composition suspension was placed onto the polished side of a glassy carbon disk. The disk was then dried for 12 h in a vacuum desiccator with an internal pressure of 5000 Pa (50 mbar).

Electrochemistry. A 0.10 M solution of H_2SO_4 was used as the electrolyte for electrochemical experiments. A 250 mL four-port glass cell was filled with electrolyte and equipped with a film-coated rotating disk electrode (RDE), a graphite rod (99% pure, Alfa Aesar) that served as a counter electrode, and a Ag/AgCl reference electrode (CH Instruments, Austin, TX). The Ag/AgCl electrode consisted of a Ag wire in 1.0 M KCl and had been calibrated against a reversible hydrogen electrode (RHE) prior to use in these experiments, with the Ag/AgCl electrode having a potential of 280 ± 2 mV vs RHE. Potentiostatic control was accomplished using a BioLogic SP-200 potentiostat (Biologic, Grenoble, France). The uncompensated cell resistance was determined from a single-point high-frequency impedance measurement and was 85% compensated by the BioLogic positive-feedback software. The RDE was rotated at a rate of 1600 rpm during the experiments. During all of the HER-catalysis experiments, the cell was saturated with H_2 (99.999%, Air Liquide, Plumsteadville, PA) by bubbling the gas through the solution.

Cyclic voltammetric scans were obtained by sweeping the applied voltage between 0.0 and -0.40 V vs RHE at a scan rate of 5 mV s^{-1}. To evaluate the stability of the films, the cyclic voltammetric scans were performed continuously over a 48 h period. The physical characterization of the films was performed after ten cycles.

The surface roughness factors for the thin films were calculated from double-layer capacitance measurements.[42-44] Current density vs potential data were acquired by sweeping the applied potential at various scan rates (20, 40, 80, 150, and 300 mV s^{-1}) in a potential range within which no Faradaic electron-transfer processes were observed (0.28–0.38 V versus RHE). The geometric capacitance of the thin films was calculated as the slope of a plot of scan rate vs current density at 0.34 V, which is the midpoint potential of the non-Faradaic region. The surface roughness factors for the thin films were calculated by dividing the measured geometric capacitance by the specific capacitance of MoS_2, which was taken as 60 μF cm^{-2}.[21, 42-44]

Scanning electron microscopy. Scanning electron micrographs were acquired with an FEI Nova electron microscope (FEI, Hillsboro, OR) at a working distance of 5.0 mm. Low-magnification micrographs (field width > 100 μm) were obtained at an accelerating voltage of 10 kV with an Everhart-Thornley detector, whereas higher magnification experiments utilized an accelerating voltage of 15 kV and a through-the-lens detector.

X-ray photoelectron spectroscopy. X-ray photoelectron spectroscopic (XPS) data for elemental composition and valence information were collected with an Axis Ultra X-ray photoelectron spectrometer (Kratos, Manchester, United Kingdom) at a base pressure < 10^{-9} Torr. Data were obtained with a monochromatic Al Kα source (1486.7 eV) and a concentric hemispherical analyzer with a pass energy of 20 eV, with the photoelectrons captured normal to the surface. Binding energies were calibrated against the "adventitious" C 1s peak (taken as 284.65 eV). Peak fitting was performed using CasaXPS software (CASA Ltd, Teignmouth, United Kingdom) assuming a Shirley background[45] and symmetric Voigt line shapes comprised of Gaussian (70%) and

Lorentzian (30%) functions. The peak fitting was constrained to maintain a 2:3 ratio between the areas of the Mo $3d_{3/2}$ and Mo $3d_{5/2}$ peaks and to maintain a 3.15 eV separation between the binding energies of those two peaks. The possibility of Se to exist in the bridging Se_2^{2-} form, analogous to what has been reported for S in MoS_3,[27] was not considered here in the interpretation of the Se XPS spectra.

Raman Spectroscopy. Raman spectra of the films were obtained with a Renishaw inVia Raman microprobe (Renishaw, Wotton Under Edge, United Kingdom) equipped with a Leica DM 2500M microscope, a Leica N Plan 50x objective (Leica, Wetzlar, Germany) (numerical aperture = 0.75), a 1800 lines/mm grating and a CCD detector configured in a 180° backscatter geometry. A 532-nm diode-pumped solid-state laser (Renishaw RL532C50) was used as the excitation and delivered a 20 μW radiant flux at the surface of the sample.

High-Resolution Transmission Electron Microscopy (HRTEM). HRTEM was performed with a Tecnai F30ST system (FEI, Hillsboro, OR) run at a voltage of 300 kV. The films were prepared by pipetting the particle suspension onto 300-mesh carbon-coated Cu grids and allowing the suspension to evaporate.

X-Ray Diffraction (XRD). XRD measurement patterns were recorded on a Bruker D8 Discover with Vantec500 area detector using Cu Kα radiation (λ = 1.5418 Å) at 50W. XRD was performed on a powder of molybdenum selenide that was synthesized by drying the precipitant of the centrifuged products.

Faradaic Efficiency Calculations. Chronopotentiometric data from the stability studies show that the total number of electrons passed in 24 hours at 10 mA cm^{-2} is 1.75 x 10^{-3} mol of electrons. Assuming a competing $2e^-$ process involving all the Mo atoms in

the film [e.g. the reduction of Mo(VI) to Mo(IV)], only 1.1 x 10^{-6} mol of e^- would be consumed; thus, the current associated with this side reaction is less than 0.1% of the total measured current. Even in the extreme hypothetical case of a competing $6e^-$ process, the side reaction would still constitute less than 0.2% of the total measured current. Thus, the faradaic yield is greater than 99%.

2.6 References

1. T. F. Jaramillo, K. P. Jorgensen, J. Bonde, J. H. Nielsen, S. Horch and I. Chorkendorff, *Science*, 2007, **317**, 100-102.

2. T. F. Jaramillo, J. Bonde, J. Zhang, B.-L. Ooi, K. Andersson, J. Ulstrup and I. Chorkendorff, *J. Phys. Chem. C*, 2008, **112**, 17492-17498.

3. J. Bonde, P. G. Moses, T. F. Jaramillo, J. K. Nørskov and I. Chorkendorff, *Faraday Discuss.*, 2009, **140**, 219-231.

4. Z. Chen, D. Cummins, B. N. Reinecke, E. Clark, M. K. Sunkara and T. F. Jaramillo, *Nano Lett.*, 2011, **11**, 4168-4175.

5. J. D. Benck, Z. Chen, L. Y. Kuritzky, A. J. Forman and T. F. Jaramillo, *ACS Catal.*, 2012, **2**, 1916-1923.

6. J. Kibsgaard, Z. Chen, B. N. Reinecke and T. F. Jaramillo, *Nat. Mater.*, 2012, **11**, 963-969.

7. D. Merki, H. Vrubel, L. Rovelli, S. Fierro and X. Hu, *Chem. Sci.*, 2012, **3**, 2515-2525.

8. H. Vrubel, D. Merki and X. Hu, *Energy Environ. Sci.*, 2012, **5**, 6136-6144.

9. H. Vrubel and X. Hu, *ACS Catal.*, 2013, 2002-2011.

10. H. Vrubel, T. Moehl, M. Gratzel and X. Hu, *Chem Commun.*, 2013, **49**, 8985-8987.

11. B. Hinnemann, P. G. Moses, J. Bonde, K. P. Jørgensen, J. H. Nielsen, S. Horch, I. Chorkendorff and J. K. Nørskov, *J. Am. Chem. Soc.*, 2005, **127**, 5308-5309.

12. J. H. Nielsen, L. Bech, K. Nielsen, Y. Tison, K. P. Jørgensen, J. L. Bonde, S. Horch, T. F. Jaramillo and I. Chorkendorff, *Surf. Sci.*, 2009, **603**, 1182-1189.

13. Y. Hou, B. L. Abrams, P. C. K. Vesborg, M. E. Björketun, K. Herbst, L. Bech, A. M. Setti, C. D. Damsgaard, T. Pedersen, O. Hansen, J. Rossmeisl, S. Dahl, J. K. Nørskov and I. Chorkendorff, *Nat. Mater.*, 2011, **10**, 434-438.

14. A. B. Laursen, S. Kegnæs, S. Dahl and I. Chorkendorff, *Energy Environ. Sci.*, 2012, **5**, 5577-5591.

15. B. Seger, A. B. Laursen, P. C. K. Vesborg, T. Pedersen, O. Hansen, S. Dahl and I. Chorkendorff, *Angew. Chem., Int. Ed.*, 2012, **51**, 9128-9131.

16. Z. Wu, B. Fang, Z. Wang, C. Wang, Z. Liu, F. Liu, W. Wang, A. Alfantazi, D. Wang and D. P. Wilkinson, *ACS Catal.*, 2013, 2101-2107.

17. M. A. Lukowski, A. S. Daniel, F. Meng, A. Forticaux, L. Li and S. Jin, *J. Am. Chem. Soc.*, 2013, **135**, 10274-10277.

18. Y. Li, H. Wang, L. Xie, Y. Liang, G. Hong and H. Dai, *J. Am. Chem. Soc.*, 2011, **133**, 7296-7299.

19. D. Kong, H. Wang, J. J. Cha, M. Pasta, K. J. Koski, J. Yao and Y. Cui, *Nano Lett.*, 2013, **13**, 1341-1347.

20. H. Wang, D. Kong, P. Johanes, J. J. Cha, G. Zheng, K. Yan, N. Liu and Y. Cui, *Nano Lett.*, 2013, **13**, 3426-3433.

21. Y. H. Chang, C. T. Lin, T. Y. Chen, C. L. Hsu, Y. H. Lee, W. Zhang, K. H. Wei and L. J. Li, *Adv. Mater.*, 2013, **25**, 756-760.

22. S. Murugesan, A. Akkineni, B. P. Chou, M. S. Glaz, D. A. Vanden Bout and K. J. Stevenson, *ACS Nano*, 2013.

23. M. L. Tang, D. C. Grauer, B. Lassalle-Kaiser, V. K. Yachandra, L. Amirav, J. R. Long, J. Yano and A. P. Alivisatos, *Angew. Chem., Int. Ed.*, 2011, **50**, 10203-10207.

24. D. Merki, S. Fierro, H. Vrubel and X. Hu, *Chem. Sci.*, 2011, **2**, 1262-1267.

25. J. M. Velazquez, F. H. Saadi, A. P. Pieterick, J. M. Spurgeon, M. P. Soriaga, B. S. Brunschwig and N. S. Lewis, *J. Electroanal. Chem.*, 2014, **716**, 45-48.

26. D. Merki and X. Hu, *Energy Environ. Sci.*, 2011, **4**, 3878-3888.

27. D. Voiry, H. Yamaguchi, J. Li, R. Silva, D. C. B. Alves, T. Fujita, M. Chen, T. Asefa, V. B. Shenoy, G. Eda and M. Chhowalla, *Nat. Mater.*, 2013, **12**, 850-855.

28. P. A. Spevack and N. S. McIntyre, *J. Phys. Chem.*, 1993, **97**, 11031-11036.

29. W. Swartz and D. M. Hercules, *Anal. Chem.*, 1971, **43**, 1774-1779.

30. W. e. Abdallah and A. E. Nelson, *J. Mater. Sci.*, 2005, **40**, 2679-2681.

31. M. Shenasa, S. Sainkar and D. Lichtman, *J. Electron Spectrosc. Relat. Phenom.*, 1986, **40**, 329-337.

32. S. N. Yannopoulos and K. S. Andrikopoulos, *J. Chem. Phys.*, 2004, **121**, 4747-4758.

33. A. Müller, E. Diemann, R. Jostes and H. Bögge, *Angew. Chem. Int. Edit.*, 1981, **20**, 934-955.

34. H. W. Wang, P. Skeldon, G. E. Thompson and G. C. Wood, *J. Mater. Sci.*, 1997, **32**, 497-502.

35. A. F. W. Holleman, Egon; Wiberg, Nils, *Lehrbuch der Anorganischen Chemie.*, Walter de Gruyter, 1985.

36. F. A. W. Cotton, Geoffrey; Murillo, Carlos A.; Bochmann, Manfred *Advanced Inorganic Chemistry (6th ed.)*, Wiley-Interscience, New York, 1999.

37. S. K. Srivastava and B. N. Avasthi, *J. Mater. Sci.*, 1993, **28**, 5032-5035.

38. F. Faraji, I. Safarik, O. P. Strausz, M. E. Torres and E. Yildirim, *Ind. Eng. Chem. Res.*, 1996, **35**, 3854-3860.

39. K. Hu, X. Hu, Y. Xu and J. Sun, *J. Mater. Sci.*, 2010, **45**, 2640-2648.

40. J. L. Brito, M. Ilija and P. Hernández, *Thermochim. Acta*, 1995, **256**, 325-338.

41. B. A. Bilal and H. Tributsch, *J. Appl. Electrochem.*, 1998, **28**, 1073-1081.

42. S. Trasatti and O. A. Petrii, *Pure Appl. Chem.*, 1991, **63**, 711-734.

43. B. E. Conway, V. Birss and J. Wojtowicz, *J. Power Sources*, 1997, **66**, 1-14.

44. R. Kötz and M. Carlen, *Electrochim. Acta*, 2000, **45**, 2483-2498.

45. D. A. Shirley, *Physical Review B*, 1972, **5**, 4709-4714.